

Development of Novel Cathode with Large Lithium Storage Mechanism Based on Pyrophosphate-Based Conversion Reaction for Rechargeable Lithium Batteries

Yongseok Lee, Jae Hyeon Jo, Hyunyoung Park, Wonseok Ko, Jungmin Kang, Seung-Taek Myung, Yang-Kook Sun,* and Jongsoo Kim*

A conversion-reaction-based nanosized $\text{Cu}_2\text{P}_2\text{O}_7$ -carbon composite is investigated as a novel cathode material with superior capacity for lithium-ion batteries. To overcome the sluggish kinetics of the conversion reaction, the nanosized $\text{Cu}_2\text{P}_2\text{O}_7$ -carbon composite is prepared by high-energy ball-milling of $\text{Cu}_2\text{P}_2\text{O}_7$ and conductive carbon to achieve simultaneous nanosizing and carbon mixing. The nanosized $\text{Cu}_2\text{P}_2\text{O}_7$ -carbon composite exhibits a large specific capacity of $\approx 355 \text{ mAh g}^{-1}$ with an average operation voltage of $\approx 2.8 \text{ V}$ (vs Li^+/Li). Moreover, even at 1C ($1\text{C} = 355 \text{ mA g}^{-1}$), the composite delivers a capacity of $\approx 215 \text{ mAh g}^{-1}$, corresponding to $\approx 60\%$ of its theoretical capacity. For 400 cycles at 1C, the nanosized $\text{Cu}_2\text{P}_2\text{O}_7$ -carbon composite exhibits capacity retention of $\approx 72\%$ compared with the initial capacity as well as high Coulombic efficiency of more than 99%. The reversible conversion reaction mechanism of the nanosized $\text{Cu}_2\text{P}_2\text{O}_7$ -carbon composite under the Li-cell system is confirmed using various techniques, including operando/ex situ X-ray diffraction, X-ray absorption near edge structure spectroscopy, extended X-ray absorption fine structure spectroscopy, and transmission electron microscopy. It is verified that $\text{Cu}_2\text{P}_2\text{O}_7$ is converted into $\text{Li}_4\text{P}_2\text{O}_7$ and metallic Cu^0 on discharge and reversibly recovered to $\text{Cu}_2\text{P}_2\text{O}_7$ on charge.

to large-scale devices, such as electric vehicles and ESSs.^[11–15] Intercalation-based electrodes have generally been considered promising for LIB cathodes, and their properties have been extensively studied.^[16,17] Increasing the specific capacity is one of the most important issues remaining for intercalation-based cathode materials for LIBs.^[18] However, the specific capacity of intercalation-based cathodes for LIBs has not yet exceeded 230 mAh g^{-1} .^[19,20] If the aim is to increase the specific capacity of electrode materials, conversion-based reactions are considered more suitable than intercalation-based reactions.^[21,22] However, most conversion-based electrode materials exhibit not only a large specific capacity of more than 300 mAh g^{-1} but also a very low average operation voltage ($<1 \text{ V}$ vs Li^+/Li).^[23] Thus, conversion-based electrode materials are usually used as anode materials.

In this study, we attempted to design a novel conversion-based cathode material with high operation voltage by maximizing

1. Introduction

Air pollution has become a more serious issue with the continued use of fossil fuels; thus, the importance of developing eco-friendly sustainable energy technologies has been recognized.^[1–4] Li-ion batteries (LIBs) are considered one of the most efficient energy storage systems (ESSs) because of their excellent energy density and high operation voltage.^[5–10] Today, LIB applications have grown from small portable electronic devices

the inductive effect through the introduction of polyanion groups.^[24,25] It has been reported that the inclusion of polyanion-based materials containing P or S with high electronegativity tends to result in higher redox potential than that of nonpolyanion-based materials because the transition metal (TM) ions are affected by the high electronegativity of the polyanion groups.^[26] Furthermore, it has been confirmed that Cu-based materials have low negative standard enthalpies of formation compared with those of other TM-based materials; therefore, higher redox potential can be attained with Cu-based materials.^[27] Thus, we supposed that the Cu-based polyanion $\text{Cu}_2\text{P}_2\text{O}_7$ can deliver high redox potential with large specific capacity of more than 230 mAh g^{-1} owing to the inductive effect of the P–O polyanion group assisted by Cu.^[28] However, the sluggish kinetics is an intrinsic issue for conversion-based materials, which implies that special treatment is required to realize the theoretical properties of $\text{Cu}_2\text{P}_2\text{O}_7$ as a cathode material for LIBs.^[29] The rate of ion diffusion is mainly determined by the length of the ion diffusion path of the material; therefore, a smaller particle size results in improved electrical performance.^[30,31] Moreover, coating with conductive carbon results in not only greatly improved electrical conductivity but also suppressed volume expansion of electrode

Y. Lee, J. H. Jo, H. Park, W. Ko, J. Kang, Prof. S.-T. Myung, Prof. J. Kim
Department of Nanotechnology and Advanced Materials Engineering
Sejong University
Seoul 05006, Republic of Korea
E-mail: jongsookim@sejong.ac.kr

Prof. Y.-K. Sun
Department of Energy Engineering
Hanyang University
Seoul 04763, Republic of Korea
E-mail: yksun@hanyang.ac.kr

 The ORCID identification number(s) for the author(s) of this article can be found under <https://doi.org/10.1002/smt.201900847>.

DOI: 10.1002/smt.201900847

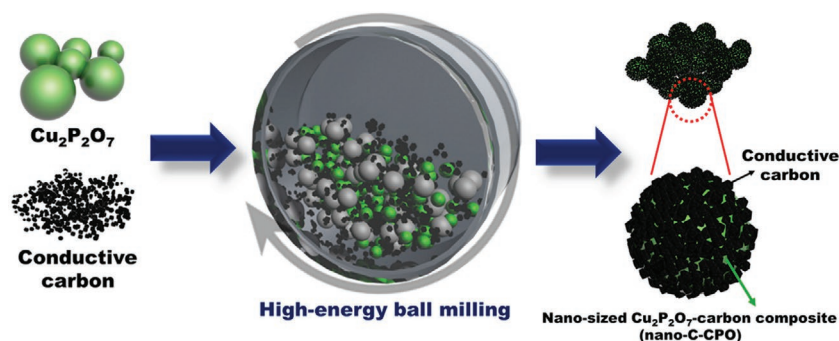


Figure 1. Scheme of nanosizing and carbon mixing of nano-C-CPO particles using high-energy ball-milling.

materials during cycling.^[32] Thus, to improve the kinetics of the conversion reaction of $\text{Cu}_2\text{P}_2\text{O}_7$ in the Li-cell system, in this work, high-energy ball-milling with conductive carbon was performed to successfully prepare a nanosized $\text{Cu}_2\text{P}_2\text{O}_7$ -conductive carbon composite (nano-C-CPO).

The nano-C-CPO electrode delivered a capacity of $\approx 355 \text{ mAh g}^{-1}$ at C/30 ($1\text{C} = 355 \text{ mA g}^{-1}$) with an average operation voltage of $\approx 2.7 \text{ V}$ (vs Li^+/Li), which is consistent with its theoretical capacity, corresponding to 4 mol Li storage per formula unit of $\text{Cu}_2\text{P}_2\text{O}_7$. The higher redox potential of $\text{Cu}_2\text{P}_2\text{O}_7$ compared with that of other conversion-based electrodes for LIBs was confirmed through first-principles calculation. Even at 10C, a specific capacity of $\approx 215 \text{ mAh g}^{-1}$ was delivered, whereas the pristine $\text{Cu}_2\text{P}_2\text{O}_7$ only delivered a specific capacity of $\approx 72 \text{ mAh g}^{-1}$ at C/30 ($1\text{C} = 355 \text{ mA g}^{-1}$). Furthermore, the nano-C-CPO retained up to $\approx 72\%$ of its initial capacity for 400 cycles at 1C. The conversion-reaction mechanism of $\text{Cu}_2\text{P}_2\text{O}_7$ under the Li-cell system ($\text{Cu}_2\text{P}_2\text{O}_7 + 4\text{Li}^+ + 4\text{e}^- \rightarrow 2\text{Cu} + \text{Li}_4\text{P}_2\text{O}_7$) was confirmed through various analyses, including operando/ex situ X-ray diffraction (XRD), ex situ X-ray absorption near edge structure (XANES) analysis, ex situ extended X-ray absorption fine structure (EXAFS) analysis, and high-resolution transmission electron microscopy (HRTEM).

2. Results and Discussion

To predict the average operation voltage of $\text{Cu}_2\text{P}_2\text{O}_7$ in the Li-cell system, we verified the formation energies of the reactants and products related to the conversion reaction of $\text{Cu}_2\text{P}_2\text{O}_7$ using first-principles calculation and then calculated the theoretical redox potential using the following equation

$$V = -\frac{2E(\text{Cu}) + E(\text{Li}_4\text{P}_2\text{O}_7) - E(\text{Cu}_2\text{P}_2\text{O}_7) - 4E(\text{Li})}{4F} \quad (1)$$

where V is the average redox potential of the conversion reaction of $\text{Cu}_2\text{P}_2\text{O}_7$, E is the formation energy of each component based on density functional theory (DFT), and F is the Faraday constant. The formation energies of each component are tabulated in Table S1 (Supporting Information). Although the $\text{Cu}_2\text{P}_2\text{O}_7$ undergoes a conversion reaction, the calculated redox potential of $\text{Cu}_2\text{P}_2\text{O}_7$ was $\approx 2.8 \text{ V}$ (vs Li^+/Li), which is higher than the average operation voltages of other conversion-based

electrodes for LIBs. We also calculated the theoretical redox potential of CuO in the Li-cell system based on the following conversion reaction: $\text{CuO} + 2\text{Li}^+ + 2\text{e}^- \rightarrow \text{Cu} + \text{Li}_2\text{O}$. The predicted average redox potential of CuO is only 1.4 V (vs Li^+/Li), which implies that the inductive effect of P-O bonding enables achievement of a high redox potential, in agreement with previous findings.^[33,34]

The nano-C-CPO was prepared by high-energy ball-milling, which can be used to simultaneously achieve nanosizing and homogeneous coating of conductive carbon, as schematically illustrated in Figure 1. In

addition, as presented in Figure S1a (Supporting Information) below, crystallinity of the 30 wt% carbon used sample is too poor with highly broad peaks unlike the other samples. In addition, when the carbon contents for preparing the nano-C-CPO composite was insufficient, the ball-milling process was not successfully proceeded, which may result in insufficient carbon-coating of particles. Figure S1b (Supporting Information) shows that the 20 wt% carbon used sample exhibits better electrochemical performances than the other samples, such as the 10 and 30 wt% carbon used samples, even though all samples had same mass ratio of carbon at manufacturing electrodes. Thus, we selected 20 wt% carbon used samples for the researches on conversion reaction of $\text{Cu}_2\text{P}_2\text{O}_7$ under the Li-cell system. Measured XRD intensity of nano-C-CPO was much lower and broader than that of pristine $\text{Cu}_2\text{P}_2\text{O}_7$, which imply that the nano-C-CPO has lower crystallinity from nanocrystal structure (Figure 2a).

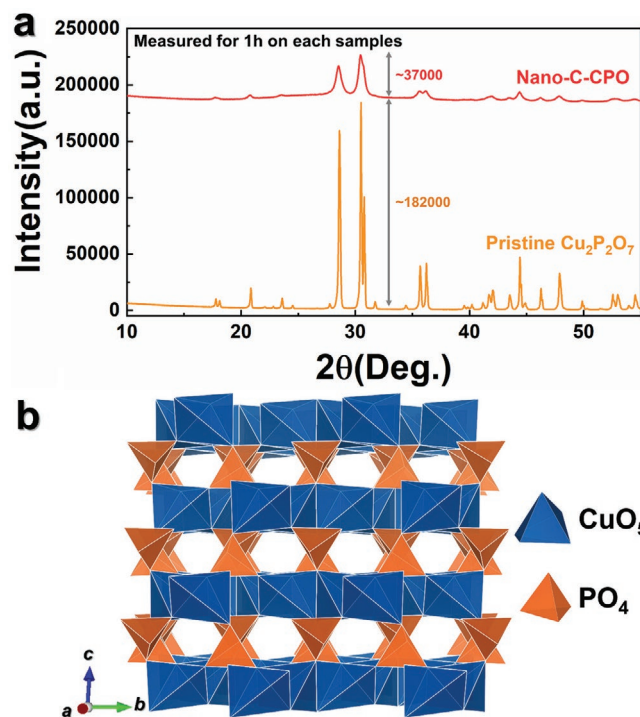


Figure 2. a) Comparing XRD intensity between nano-C-CPO and pristine $\text{Cu}_2\text{P}_2\text{O}_7$ using XRD patterns which measured for 1 h on each samples. b) Crystal structure of nano-C-CPO composite.

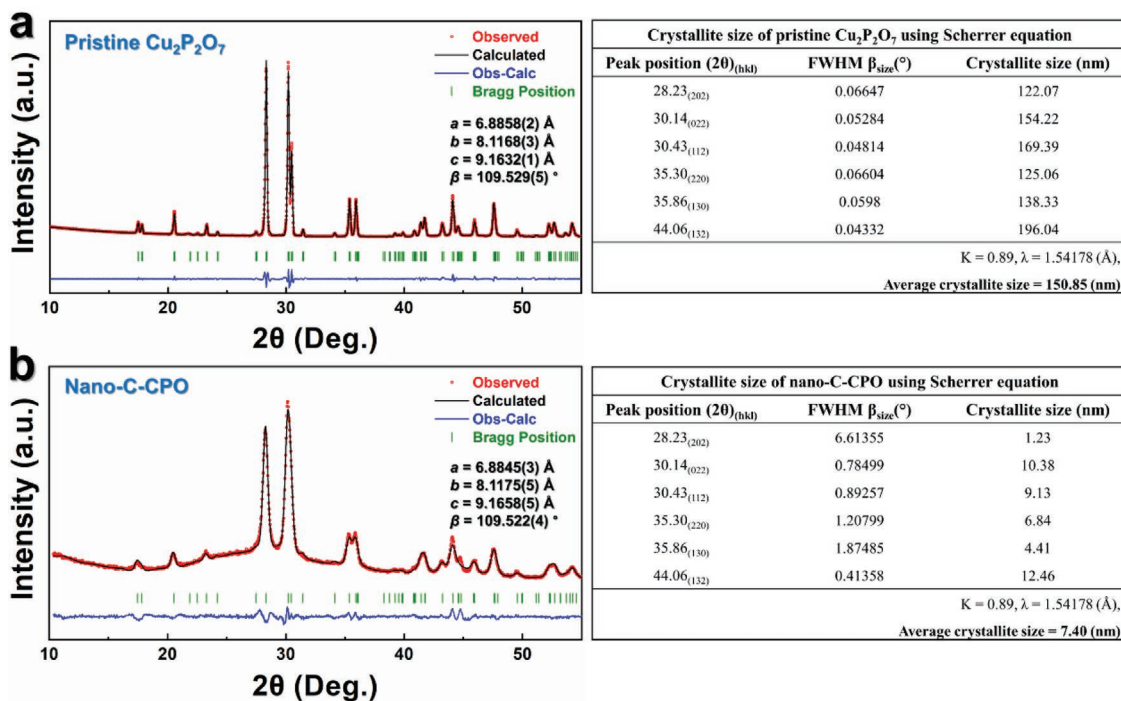


Figure 3. Refined XRD pattern and crystallite size using Scherrer equation for selected $h k l$ reflections of a) pristine $\text{Cu}_2\text{P}_2\text{O}_7$ ($R_p = 3.11\%$, $R_1 = 3.84\%$, $R_f = 4.03\%$, and $\chi^2 = 7.95\%$); b) nano-C-CPO composite ($R_p = 2.51\%$, $R_1 = 4.45\%$, $R_f = 3.49\%$, and $\chi^2 = 2.80\%$) XRD pattern.

Although the high energy was applied on $\text{Cu}_2\text{P}_2\text{O}_7$ during ball-milling, nano-C-CPO maintained stabilized monoclinic structure as represented at Figure 2b. In addition, we compared the crystal structure between the as-prepared sample and the sample exposed in air-condition for 1 week through XRD analyses. As presented in Figure S2 (Supporting Information), the crystal structure of $\text{Cu}_2\text{P}_2\text{O}_7$ is well retained without severe change after the exposure and any hydrated phases on $\text{Cu}_2\text{P}_2\text{O}_7$ by the water-adsorption were not detected. To verify the crystallinity of the nano-C-CPO, Rietveld refinement of the XRD patterns of nano-C-CPO, and pristine $\text{Cu}_2\text{P}_2\text{O}_7$ was performed (Figure 3a,b; and Table S2, Supporting Information). The nano-C-CPO exhibited a pure crystal structure of $\text{Cu}_2\text{P}_2\text{O}_7$ with $C12/c1$ space group, even though high energy was applied and conductive carbon was coated on the particles by ball-milling. The calculated lattice parameters of the nano-C-CPO were $a = 6.8845(3)$ Å, $b = 8.1175(5)$ Å, $c = 9.1658(5)$ Å, and $\beta = 109.522(4)^\circ$, which is well matched with those of pristine $\text{Cu}_2\text{P}_2\text{O}_7$ and the values reported in the literature.^[35,36] To confirm the decreased particle size of the nano-C-CPO, we compared the crystallite sizes of the nano-C-CPO and pristine $\text{Cu}_2\text{P}_2\text{O}_7$ using the Scherrer equation and associated XRD patterns. In addition, crystallite size indicates the size of coherently diffracting regions or domains of a material, and particle size indicates the size of single particle or agglomerated particles.^[37–40] The average crystallite size of the nano-C-CPO was only ≈ 7.40 nm, which is much smaller than that of the pristine $\text{Cu}_2\text{P}_2\text{O}_7$. To verify the difference of crystallite size of each samples in detail, we compared the morphologies of the nano-C-CPO and pristine $\text{Cu}_2\text{P}_2\text{O}_7$ using scanning electron microscopy (SEM). As shown in Figure 4a,b, it was verified that the nano-C-CPO had a much smaller particle size than the pristine $\text{Cu}_2\text{P}_2\text{O}_7$ with microscale particle size. Thus,

the particle size was greatly decreased through the high-energy ball-milling. In addition, the bright-field transmission electron microscopy (TEM) image of the nano-C-CPO shows the presence of carbon on the $\text{Cu}_2\text{P}_2\text{O}_7$ particle after the high-energy ball-milling (Figure S3, Supporting Information). Furthermore,

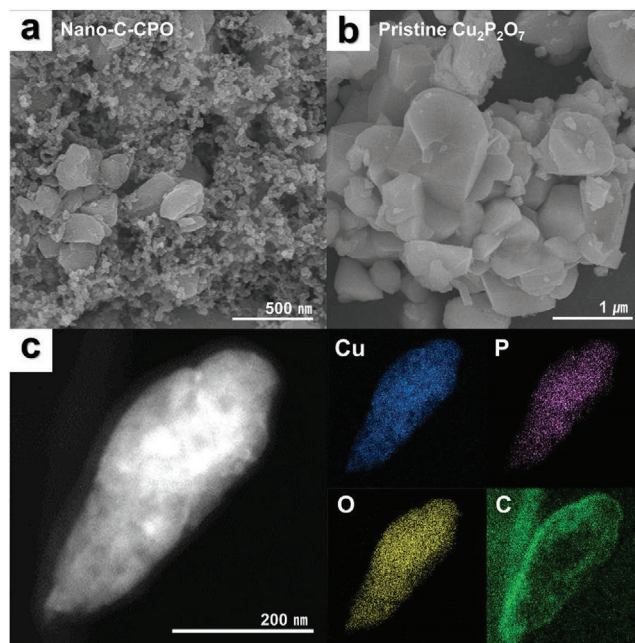


Figure 4. SEM image of a) nano-C-CPO composite, b) pristine $\text{Cu}_2\text{P}_2\text{O}_7$, c) EDS elemental mapping (Cu: blue, P: purple, O: yellow, C: green) of fresh nano-C-CPO composite.

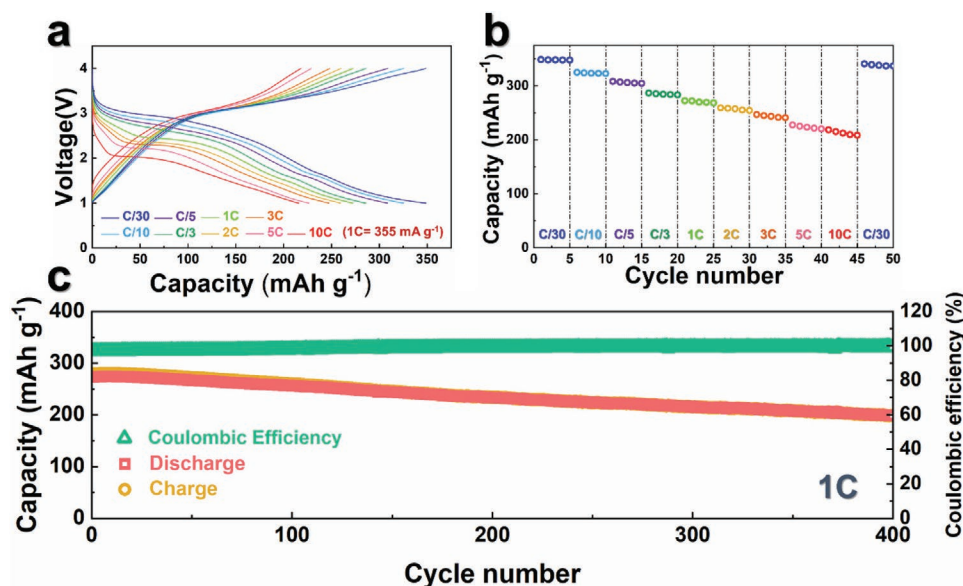


Figure 5. a) Power-capability of nano-C-CPO at various current rates. b) Rate performance of nano-C-CPO. c) Cyclic performance and Coulombic efficiency of nano-C-CPO over 400 cycles at 1C after 1 cycle at C/5.

the atomic composition of the nano-C-CPO including Cu, P, O, and C and its homogeneous carbon-coated morphology were identified through TEM with elemental mappings using energy-dispersive X-ray spectroscopy (EDS) (Figure 4c). The total carbon content of ≈ 20 wt% in the nano-C-CPO was determined through thermogravimetric analysis (Figure S4, Supporting Information). In addition, it was verified through electrochemical impedance spectroscopy analysis that the nano-C-CPO exhibited a lower charge-transfer resistance than the pristine $\text{Cu}_2\text{P}_2\text{O}_7$, indicating the highly enhanced electrical conductivity of the nano-C-CPO achieved through nanosizing and carbon coating (Figure S5, Supporting Information). Thus, because the highly reduced crystallite size and homogeneous carbon coating effectively facilitated electron transfer, resulting in enhanced electrical conductivity and preventing severe volume expansion during the conversion reaction, we speculated that the nano-C-CPO exhibited greatly improved electrochemical performance compared with that of the pristine $\text{Cu}_2\text{P}_2\text{O}_7$.

The electrochemical performances of the nano-C-CPO and pristine $\text{Cu}_2\text{P}_2\text{O}_7$ were evaluated in Li cells in the voltage range of 1–4 V (vs Li^+/Li) using Li metal as the counter electrode and 1.2 M LiPF_6 in EC:DMC = 3:7 (v/v) as the electrolyte. At C/30 ($1\text{C} = 355 \text{ mA g}^{-1}$), the specific capacity of the nano-C-CPO was $\approx 355 \text{ mAh g}^{-1}$, which is consistent with the theoretical capacity of $\text{Cu}_2\text{P}_2\text{O}_7$ corresponding to 4 mol Li ion storage per formula unit of $\text{Cu}_2\text{P}_2\text{O}_7$ (Figure 5a,b). However, for the pristine $\text{Cu}_2\text{P}_2\text{O}_7$, the specific capacity was only $\approx 71 \text{ mAh g}^{-1}$ under the same conditions (Figure S6, Supporting Information), indicating that the electrochemical performance of $\text{Cu}_2\text{P}_2\text{O}_7$ was greatly enhanced by the simultaneous nanosizing and carbon coating. Moreover, we performed cyclic voltammograms (CVs) measurement to investigate electrochemical behaviors of pristine $\text{Cu}_2\text{P}_2\text{O}_7$ and nano-C-CPO electrodes. As shown in Figure S7 (Supporting Information), we measured the CV curves of pristine $\text{Cu}_2\text{P}_2\text{O}_7$ and nano-C-CPO electrodes. Unlike the

CV curves of the nano-C-CPO electrode showing well-maintained CV profiles for several cycles, the CV curve of pristine $\text{Cu}_2\text{P}_2\text{O}_7$ are drastically decayed after initial cycling, which indicates the poor electrochemical performances of pristine $\text{Cu}_2\text{P}_2\text{O}_7$. In particular, the average operation voltage of the nano-C-CPO was verified to be $\approx 2.8 \text{ V}$ (vs Li^+/Li), which is much higher than that of other conversion-based electrodes for LIBs,^[41,42] and this result agreed well with the first-principles calculation. Furthermore, even at 5C, the specific capacity of the nano-C-CPO was $\approx 228 \text{ mAh g}^{-1}$, corresponding to $\approx 64\%$ of its theoretical capacity. For 400 cycles at 1C, the nano-C-CPO exhibited not only outstanding capacity retention of $\approx 72\%$ compared with the initial discharge capacity but also high Coulombic efficiency of more than 99% (Figure 5c; and Figure S8a, Supporting Information). The excellent cyclability of the nano-C-CPO was also confirmed for 400 charge/discharge cycles at 2C, with capacity retention of $\approx 70\%$ (Figure S8b, Supporting Information). Through XRD, SEM, and TEM analyses, we confirmed that the crystal structure and morphology of the nano-C-CPO were well retained without severe degradation despite the long cycling test (Figure S9, Supporting Information). We speculated that the outstanding cycle performance of the nano-C-CPO resulted from the homogenous carbon coating of $\text{Cu}_2\text{P}_2\text{O}_7$ particles, which can act as a buffer, preventing large volume change or structural deformation during repeated charge/discharge processes. Unlike the nano-C-CPO, the pristine $\text{Cu}_2\text{P}_2\text{O}_7$ electrode delivered poor cyclability with severe capacity fading after several cycles (Figure S10, Supporting Information). In addition, to verify the possibility of applying nano-C-CPO as a cathode in a real LIB system, we performed a full-cell test using a lithiated graphite anode. We prepared the graphite electrode with consideration of the capacity difference between the nano-C-CPO ($\approx 355 \text{ mAh g}^{-1}$) and graphite ($\approx 372 \text{ mAh g}^{-1}$). As shown in Figure 6, the full-cell of nano-C-CPO/graphite was tested at 1C ($1\text{C} = 355 \text{ mA g}^{-1}$) in the voltage range of

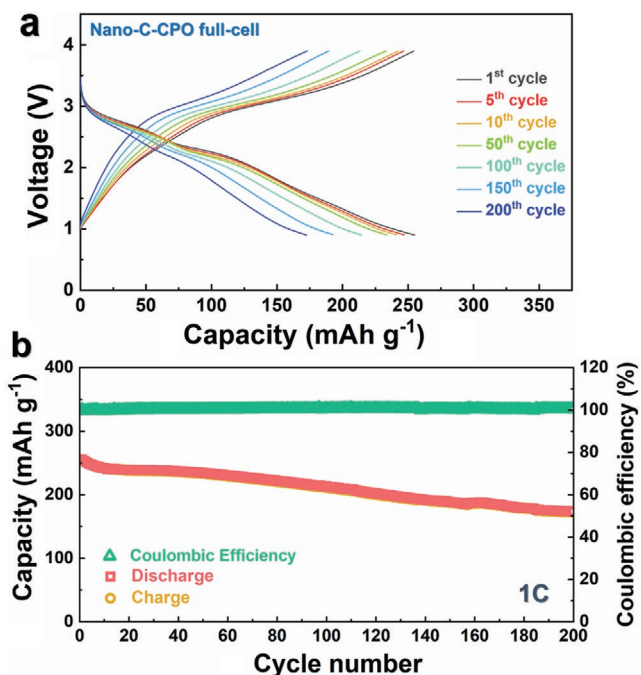


Figure 6. a) Charge/discharge curves of nano-C-CPO full-cell at 1, 5, 10, 50, 100, 150, and 200th over 200 cycles at 1C after 1 cycle at C/5. b) Cyclic performance and Coulombic efficiency of nano-C-CPO full-cell over 200 cycles at 1C after 1 cycle at C/5.

0.9–3.9 V for 200 cycles, delivering an initial specific capacity of $\approx 255 \text{ mAh g}^{-1}$. For 200 cycles at 1C, the full-cell exhibited outstanding capacity retention of $\approx 68\%$ compared with its

initial specific capacity. In addition, Table S3 (Supporting Information) showed electrochemical performance of nano-C-CPO compared to other cathode materials for LIBs.^[41,43–46] The results indicate that nano-C-CPO can be considered a promising cathode for high-energy LIBs.

To understand the conversion reaction mechanism of $\text{Cu}_2\text{P}_2\text{O}_7$ in the Li-cell system, we performed operando XRD analysis (Figure 7a). During discharging to 1.0 V (vs Li^+/Li), the XRD peak of $\text{Cu}_2\text{P}_2\text{O}_7$ at 30° disappeared, and new peaks appeared at 20° and 43° , corresponding to the (100) and (10 $\bar{2}$) peaks of $\text{Li}_4\text{P}_2\text{O}_7$ and (111) peak of metallic Cu^0 . During charging to 4.0 V (vs Li^+/Li), the XRD peaks of $\text{Cu}_2\text{P}_2\text{O}_7$ at 30° were recovered with simultaneous disappearance of the peaks related to the $\text{Li}_4\text{P}_2\text{O}_7$ and Cu^0 phases. In addition, it is supposed that difficulty of detection on coexistence of $\text{Cu}_2\text{P}_2\text{O}_7$, $\text{Li}_4\text{P}_2\text{O}_7$, and Cu^0 in the Operando XRD patterns results from the growth rate of crystalline during conversion reaction and the detection limit of XRD. This conversion reaction of $\text{Cu}_2\text{P}_2\text{O}_7$ in the Li-cell system was confirmed by ex situ XRD analysis (Figure 7b; and Figure S11, Supporting Information). The results indicated that the $\text{Cu}_2\text{P}_2\text{O}_7$ undergoes a reversible conversion reaction based on the following reaction: $\text{Cu}_2\text{P}_2\text{O}_7 + 4\text{Li}^+ + \text{e}^- \leftrightarrow \text{Li}_4\text{P}_2\text{O}_7 + \text{Cu}^0$. In addition, formation of new compounds containing Cu^+ ions, such as Cu_2O , was not detected in the Operando XRD analyses, which indicates that the conversion reaction on $\text{Cu}_2\text{P}_2\text{O}_7$ under the Li-cell system is rapidly proceeded from Cu^{2+} to metallic Cu^0 . In addition, we investigated the redox reaction mechanism of $\text{Cu}_2\text{P}_2\text{O}_7$ with the conversion reaction during charge/discharge using ex situ XANES and EXAFS analyses. As shown in Figure 7c, the Cu K-edge spectra were shifted to lower energy during discharge, indicating full reduction from Cu^{2+} to Cu^0 .

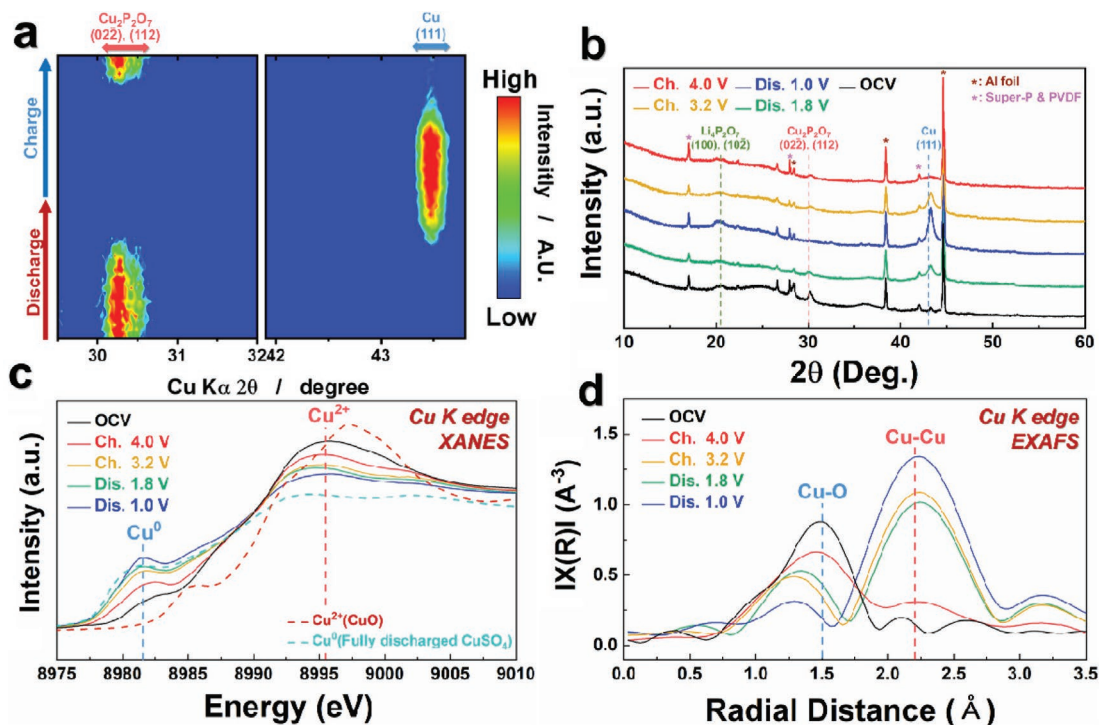


Figure 7. a) Operando and b) ex situ XRD patterns of nano-C-CPO electrode during the initial cycle. Cu K-edge c) XANES and d) EXAFS spectra of nano-C-CPO.

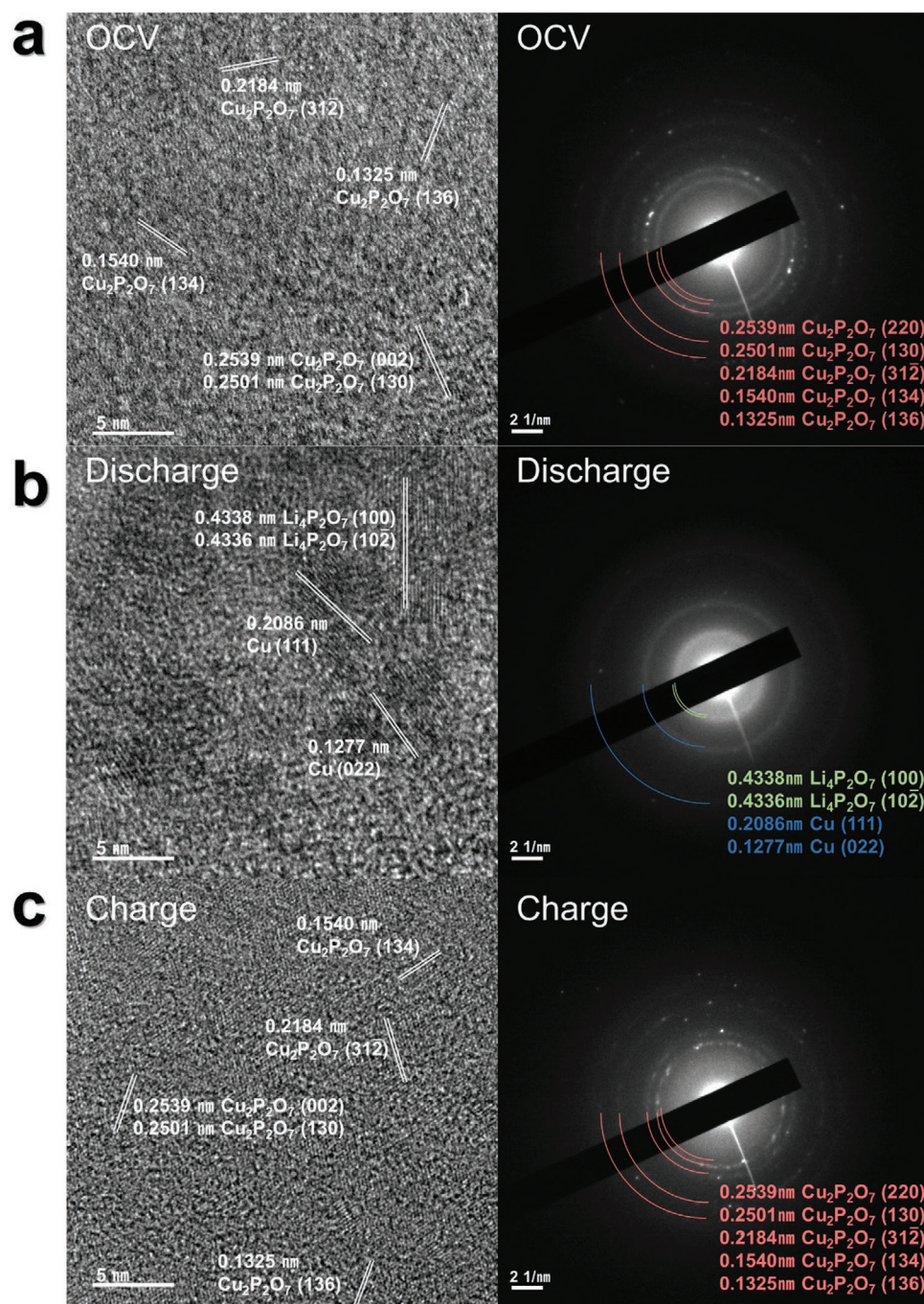


Figure 8. HRTEM image and SAED pattern of a) fresh, b) discharged, and c) charged nano-C-CPO composite.

Then, the Cu K-edge spectra returned to the original energy level during charge, indicating that Cu^0 was re-oxidized to Cu^{2+} . Moreover, Fourier transform (FT) of the EXAFS spectra was performed to confirm the transition of Cu–O and Cu–Cu bonds (Figure 7d). As the discharge progressed, the intensity of the Cu–O interaction decreased, and the Cu–Cu bond substantially grew because of the formation of metallic Cu^0 . During the charging process, the intensity of the Cu–Cu bonding decreased while the Cu–O interaction became strong.^[47,48] These ex situ XANES and EXAFS results agree well with the

operando/ex situ XRD analyses showing the formation and decomposition of $\text{Cu}_2\text{P}_2\text{O}_7$, $\text{Li}_4\text{P}_2\text{O}_7$, and metallic Cu^0 during charge/discharge. In addition, through HRTEM and selected-area electron diffraction (SAED) analyses, we confirmed that the fully discharged nano-C-CPO electrode is composed of metallic Cu^0 and $\text{Li}_4\text{P}_2\text{O}_7$ phases, unlike the pristine and fully charged nano-C-CPO electrodes, which consist of the $\text{Cu}_2\text{P}_2\text{O}_7$ phase (Figure 8). In addition, Figure S12 (Supporting Information) shows the elements distribution on fresh, discharged, and charged nano-C-CPO electrodes.

3. Conclusion

We successfully prepared a nano-C–CPO composite as a novel conversion-based cathode for LIBs using a simple high-energy ball-milling process and investigated its electrochemical performance. The nano-C–CPO delivered outstanding electrochemical performance as a cathode for high-energy LIBs with enhanced electrical conductivity and shortened diffusion paths achieved by nanosizing and homogenous carbon coating. The nano-C–CPO delivered a large specific capacity of ≈ 355 mAh g⁻¹ with an average operation voltage of ≈ 2.8 V (vs Li⁺/Li) at C/30 (1C = 355 mA g⁻¹), which corresponds to the theoretical capacity of Cu₂P₂O₇ based on 4 mol Li⁺ storage per formula unit of Cu₂P₂O₇. Even at 5C (1C = 355 mA g⁻¹), a specific capacity of ≈ 228 mAh g⁻¹ was delivered, corresponding to $\approx 64\%$ of its theoretical capacity. This result indicates the outstanding power-capability of the nano-C–CPO. Furthermore, the nano-C–CPO exhibited superior cyclability with capacity retention of $\approx 72\%$ compared with its initial capacity for 400 cycles. Through first-principles calculation and various analyses including operando/ex situ XRD, ex situ XANES/EXAFS, and ex situ HRTEM, we confirmed two important properties of the nano-C–CPO in the Li-cell system: 1) the higher redox potential of Cu₂P₂O₇ compared with that of other conversion-based electrodes for LIBs because of the inductive effect of P–O in the structure and 2) the reversible conversion reaction of Cu₂P₂O₇ + 4Li⁺ + 4e⁻ \leftrightarrow 2Cu⁰ + Li₄P₂O₇. Our findings provide insight to help overcome the energy density limit of cathode materials for LIBs.

4. Experimental Section

Preparation of Nano-C–CPO: CuO (Sigma-Aldrich, 99%) and NH₄H₂(PO₄) (Sigma-Aldrich, 98%) precursors were used to prepare the crystalline Cu₂P₂O₇ powders. The precursors were mixed using wet ball-milling at 300 rpm for 12 h with acetone. The mixed powder was dried at 80 °C for 12 h with stirring on a hot plate. After evaporation, the precursors were ground into a fine powder, and the powder was calcined at 850 °C for 10 h in air. The color of the synthesized Cu₂P₂O₇ was light emerald. The pristine Cu₂P₂O₇ was mixed with carbon using high-energy ball-milling of 80 wt% Cu₂P₂O₇ and 19 wt% Super P carbon black. The powders were placed in a nitride jar with 30 balls and ball milled at 500 rpm for 15 h. Finally, the Cu₂P₂O₇ was mixed with 1 wt% carbon nanotubes using high-energy ball-milling at 100 rpm for 12 h.

Materials Characterization: The nano-C–CPO powders were characterized using XRD (PANalytical) with Cu K α radiation (wavelength = 1.54 178 Å). The 2 θ range was 10°–60° with a time per step of 0.13. The FullProf Rietveld program was used to analyze the XRD data. The morphology of the materials was examined using SEM (SU-8010). The overall conversion reaction was revealed using HR-TEM (JEM-3010) at the National Center for Inter-University Research Facilities (NCIRF) at Seoul National University. XANES spectroscopy was performed at beamline 6D at the 3.0-GeV Pohang Light Source. The impedance of each sample was analyzed from 5 to 500 MHz using a multichannel impedance analyzer system (VSP-300, Bio-Logic, Grenoble, France). The Operando XRD patterns of nano-C–CPO were analyzed using XRD (PANalytical, Empyrean) with Cu K α radiation ($\lambda = 1.54$ 178 Å) in the 2 θ range of 29°–44° with a step size of 0.026°. During operando XRD experiments, the Operando battery cell (ISBC) was used for XRD made by PANalytical with PDC TECH. The cell was measured at C/30 (1C = 355 mA g⁻¹) in the voltage range of 1.0–4.0 V

with a Li counter electrode, a separator (Celgard 2400), and 1.2 M LiPF₆ in EC:DMC = 3:7(v/v) as the electrolyte. To protect the cell system from water, a beryllium (Be) window was used.

Electrochemical Characterization: The electrodes were fabricated from a slurry of 85 wt% nano-C–CPO composite, 5 wt% Super-P carbon, and 10 wt% polyvinylidene fluoride (PVDF) binder in *N*-methyl-2-pyrrolidone. Thus, the nano-C–CPO electrode consisted of 68 wt% Cu₂P₂O₇ as the active material, 22 wt% conductive carbon, and 10 wt% PVDF binder. For fair comparison of the electrochemical performance of the nano-C–CPO and pristine Cu₂P₂O₇ electrodes, the same mass ratio of 68 wt% Cu₂P₂O₇, 22 wt% conductive carbon, and 10 wt% PVDF binder for preparation of both electrodes was applied. The slurry was applied on Al foil using a doctor blade and dried in an oven at 110 °C for 12 h. R2032 cells were assembled in an Ar-filled glove box using the Cu₂P₂O₇ composite electrode, a Li counter electrode, a separator (Celgard 2400), and 1.2 M LiPF₆ in EC:DMC = 3:7(v/v) as the electrolyte. The electrochemical performances of the cells were evaluated by charging and discharging in the voltage range of 1.0–4.0 V at 30 °C using an automatic battery charge/discharge test system (WBCS 3000, WonATech). The area current rates at each rate capacities were 0.02(C/30), 0.07(C/10), 0.14(C/5), 0.23(C3), 0.71(1C), 1.42(2C), 2.13(3C), 3.55(5C), and 7.1(10C) mA cm⁻².

Fabrication of Full-Cells: The full-cells were fabricated using commercial graphite (Aldrich, powder, >20 μ m) as the anode. The graphite electrode was fabricated using the same procedure and ratio as the Cu₂P₂O₇ electrode except for the use of Cu foil. To minimize the irreversibility of graphite, the graphite electrode was precycled by direct contact with Li metal in 1.2 M LiPF₆ in EC:DMC = 3:7(v/v) electrolyte. Finally, R2032 coin-type full-cells were assembled with the Cu₂P₂O₇ cathode and precycled graphite carbon anode (capacity ratio of negative and positive electrodes of ≈ 1.2) in an Ar-filled glove box.

Computational Details: DFT calculations^[49] were performed using the Vienna Ab Initio Simulation Package (VASP). Projector-augmented wave (PAW) pseudopotentials were used^[50] with a plane-wave basis set, as implemented in VASP. Perdew–Burke–Ernzerhof parametrization of the generalized gradient approximation^[51,52] was used for the exchange–correlation functional. All the calculations were performed with an energy cutoff of 520 eV until the remaining force in the system converged to less than 0.02 eV Å⁻¹ per unit cell. The parameters reported in the Materials Project database,^[53] such as the U values and energy cutoff values, were used for the DFT calculation.

Supporting Information

Supporting Information is available from the Wiley Online Library or from the author.

Acknowledgements

This research was supported by the Next Generation Engineering Researcher Program of the National Research Foundation of Korea funded by the Ministry of Science and ICT of Korea (No. NRF-2019H1D8A2106002), General Research Program of the National Research Foundation of Korea funded by the Ministry of Science and ICT of Korea (No. NRF-2019R1F1A1063415), the Radiation Technology R&D program of the National Research Foundation of Korea funded by the Ministry of Science and ICT of Korea (No. NRF-2019M2A2A6A05102365) and International Research & Development Program of the National Research Foundation of Korea funded by the Ministry of Science and ICT of Korea (No. NRF-2018K2A9A2A12000230).

Conflict of Interest

The authors declare no conflict of interest.

Keywords

carbon mixing, cathodes, conversion reactions, first-principles calculations, nanosizing

Received: December 9, 2019

Revised: January 9, 2020

Published online: February 5, 2020

- [1] J. M. Tarascon, M. Armand, *Nature* **2001**, 414, 359.
- [2] M. Armand, J. M. Tarascon, *Nature* **2008**, 451, 652.
- [3] L. L. Wang, B. B. Chen, J. Ma, G. L. Cui, L. Q. Chen, *Chem. Soc. Rev.* **2018**, 47, 6505.
- [4] W. Ko, J. K. Yoo, H. Park, Y. Lee, H. Kim, Y. Oh, S. T. Myung, J. Kim, *J. Power Sources* **2019**, 432, 1.
- [5] J. Y. Hwang, S. J. Park, C. S. Yoon, Y. K. Sun, *Energy Environ. Sci.* **2019**, 12, 2174.
- [6] A. K. Padhi, K. S. Nanjundaswamy, C. Masquelier, J. B. Goodenough, *J. Electrochem. Soc.* **1997**, 144, 2581.
- [7] L. L. Wang, J. Ma, C. Wang, X. R. Yu, R. Liu, F. Jiang, X. W. Sun, A. B. Du, X. H. Zhou, G. L. Cui, *Adv. Sci.* **2019**, 6, 11.
- [8] J. Kim, H. Kim, S. T. Myung, J. K. Yoo, S. Lee, *J. Power Sources* **2018**, 374, 55.
- [9] X. H. Xia, Y. Q. Zhang, D. L. Chao, C. Guan, Y. J. Zhang, L. Li, X. Ge, I. M. Bacht, J. P. Tu, H. J. Fan, *Nanoscale* **2014**, 6, 5008.
- [10] J. H. Jo, J. U. Choi, M. K. Cho, Y. Aniskevich, H. Kim, G. Ragoisha, E. Streltsov, J. Kim, S. T. Myung, *Adv. Energy Mater.* **2019**, 9, 1900603.
- [11] Y. Zhong, X. H. Xia, F. Shi, J. Y. Zhan, J. P. Tu, H. J. Fan, *Adv. Sci.* **2016**, 3, 1500286.
- [12] H. J. Kim, A. Konarov, J. H. Jo, J. U. Choi, K. Ihm, H. K. Lee, J. Kim, S. T. Myung, *Adv. Energy Mater.* **2019**, 9, 1901181.
- [13] H. Park, J. K. Yoo, W. Ko, Y. Lee, I. Park, S. T. Myung, J. Kim, *J. Power Sources* **2019**, 434, 226750.
- [14] A. Konarov, H. J. Kim, N. Voronina, Z. Bakenov, S. T. Myung, *ACS Appl. Mater. Interfaces* **2019**, 11, 28928.
- [15] J. U. Choi, Y. J. Park, J. H. Jo, L. Y. Kuo, P. Kaghazchi, S. T. Myung, *ACS Appl. Mater. Interfaces* **2018**, 10, 40978.
- [16] Y. Oumellal, A. Rougier, G. A. Nazri, J. M. Tarascon, L. Aymard, *Nat. Mater.* **2008**, 7, 916.
- [17] B. Dunn, H. Kamath, J. M. Tarascon, *Science* **2011**, 334, 928.
- [18] J. S. Park, J. Kim, W. B. Park, Y. K. Sun, S. T. Myung, *ACS Appl. Mater. Interfaces* **2017**, 9, 40307.
- [19] R. J. Chen, T. L. Zhao, X. X. Zhang, L. Li, F. Wu, *Nanoscale Horiz.* **2016**, 1, 423.
- [20] N. Nitta, F. X. Wu, J. T. Lee, G. Yushin, *Mater. Today* **2015**, 18, 252.
- [21] F. X. Wu, G. Yushin, *Energy Environ. Sci.* **2017**, 10, 435.
- [22] L. S. Li, F. Meng, S. Jin, *Nano Lett.* **2012**, 12, 6030.
- [23] S. H. Yu, X. R. Feng, N. Zhang, J. Seok, H. D. Abruna, *Acc. Chem. Res.* **2018**, 51, 273.
- [24] J. Kim, H. Kim, I. Park, Y. U. Park, J. K. Yoo, K. Y. Park, S. Lee, K. Kang, *Energy Environ. Sci.* **2013**, 6, 830.
- [25] Y. Lee, J. K. Yoo, Y. Oh, H. Park, W. Go, S. T. Myung, J. Kim, *J. Mater. Chem. A* **2018**, 6, 17571.
- [26] K. Y. Park, I. Park, H. Kim, H. D. Lim, J. Hong, J. Kim, K. Kang, *Chem. Mater.* **2014**, 26, 5345.
- [27] J. Kim, H. Kim, K. Kang, *Adv. Energy Mater.* **2018**, 8, 1702646.
- [28] Y. Lee, J. K. Yoo, J. H. Jo, H. Park, C. H. Jo, W. Ko, H. Yashiro, S. T. Myung, J. Kim, *ACS Nano* **2019**, 13, 11707.
- [29] M. K. Cho, J. H. Jo, J. U. Choi, J. Kim, H. Yashiro, S. Yuan, L. Y. Shi, Y. K. Sun, S. T. Myung, *Nano Energy* **2017**, 41, 687.
- [30] Y. G. Wang, Y. R. Wang, E. J. Hosono, K. X. Wang, H. S. Zhou, *Angew. Chem., Int. Ed.* **2008**, 47, 7461.
- [31] H. H. Lyu, B. Gao, F. He, C. Ding, J. C. Tang, J. C. Crittenden, *ACS Sustainable Chem. Eng.* **2017**, 5, 9568.
- [32] X. D. Liu, H. T. Liu, Y. M. Zhao, Y. Z. Dong, Q. H. Fan, Q. Kuang, *Langmuir* **2016**, 32, 12593.
- [33] J. Kim, J. K. Yoo, Y. S. Jung, K. Kang, *Adv. Energy Mater.* **2013**, 3, 1004.
- [34] J. Kim, G. Yoon, H. Kim, Y. U. Park, K. Kang, *Chem. Mater.* **2018**, 30, 3683.
- [35] K. Pogorzelec-Glaser, A. Pietraszko, B. Hilczner, M. Polomska, *Phase Transitions* **2006**, 79, 535.
- [36] A. Karaphun, P. Chirawatkul, S. Maensiri, E. Swatsitang, *J. Sol-Gel Sci. Technol.* **2018**, 88, 407.
- [37] P. E. Tomaszewski, *Phase Transitions* **2013**, 86, 260.
- [38] J. I. Langford, D. Louer, P. Scardi, *J. Appl. Crystallogr.* **2000**, 33, 964.
- [39] D. Martinez-Blanco, P. Gorria, J. A. Blanco, M. J. Perez, J. Campo, *J. Phys.: Condens. Matter* **2008**, 20, 335213.
- [40] A. Guinier, G. Fournet, *Small-Angle Scattering of X-Rays*, Wiley, New York **1955**, pp. 161–166.
- [41] X. Y. Zhou, H. X. Sun, H. C. Zhou, J. Ding, Z. L. Xu, W. J. Bin, J. J. Tang, J. Yang, *J. Electroanal. Chem.* **2018**, 810, 41.
- [42] K. Jian, Z. H. Chen, X. B. Meng, *ChemElectroChem* **2019**, 6, 2825.
- [43] X. Xu, L. Z. Xiang, L. G. Wang, J. Y. Jian, C. Y. Du, X. S. He, H. Huo, X. Q. Cheng, G. P. Yin, *J. Mater. Chem. A* **2019**, 7, 7728.
- [44] P. R. Ilango, K. Prasanna, S. J. Do, Y. N. Jo, C. W. Lee, *Sci. Rep.* **2016**, 6, 29826.
- [45] R. Muruganatham, M. Sivakumar, R. Subadevi, S. Ramaprabhu, N. L. Wu, *Electron. Mater. Lett.* **2015**, 11, 841.
- [46] L. W. Sun, Z. S. Zhang, X. F. Hu, H. Y. Tian, Y. B. Zhang, X. G. Yang, *J. Electrochem. Soc.* **2019**, 166, A1793.
- [47] J. A. Rodriguez, J. C. Hanson, D. Stacchiola, S. D. Senanayake, *Phys. Chem. Chem. Phys.* **2013**, 15, 12004.
- [48] E. B. Fox, S. Velu, M. H. Engelhard, Y. H. Chin, J. T. Miller, J. Kropf, C. S. Song, *J. Catal.* **2008**, 260, 358.
- [49] G. Kresse, J. Furthmuller, *Comput. Mater. Sci.* **1996**, 6, 15.
- [50] P. E. Blochl, *Phys. Rev. B* **1994**, 50, 17953.
- [51] J. P. Perdew, K. Burke, M. Ernzerhof, *Phys. Rev. Lett.* **1996**, 77, 3865.
- [52] V. I. Anisimov, F. Aryasetiawan, A. I. Lichtenstein, *J. Phys.: Condens. Matter* **1997**, 9, 767.
- [53] A. Jain, S. P. Ong, G. Hautier, W. Chen, W. D. Richards, S. Dacek, S. Cholia, D. Gunter, D. Skinner, G. Ceder, K. A. Persson, *APL Mater.* **2013**, 1, 011002.